ACS Catalysis

Research Article

pubs.acs.org/acscatalysis

High-Performance Dealloyed PtCu/CuNW Oxygen Reduction Reaction Catalyst for Proton Exchange Membrane Fuel Cells

Jarrid A. Wittkopf, Jie Zheng, and Yushan Yan*

Department of Chemical and Biomolecular Engineering, Center for Catalytic Science and Technology, University of Delaware, 150 Academy Street, Newark, Delaware 19716, United States

Supporting Information

ABSTRACT: One major barrier to fuel cell commercialization is the high cost of oxygen reduction reaction catalysts. Current catalysts are predominantly supported Pt nanoparticles. These nanoparticles show high surface area but low specific activity and durability. A transition to unsupported catalysts possessing an extended surface would improve both specific activity and durability and in turn cost-effectiveness when high surface area can be achieved. Platinum-coated copper nanowires (Pt/CuNW) exemplify these advantages. In this study, postsynthetic processing is used to further improve the performance of Pt/CuNW catalyst. Specifically, annealing followed by electrochemical dealloying enhances activity through geometric lattice tuning. The resultant bimetallic PtCu/CuNW catalyst yields specific and mass activities (SA and MA) of 2.65 mA cm_{Pt}^{-2} and 1.24 A mg_{Pt}^{-1}, surpassing the respective Department of Energy (DOE) benchmarks of 0.72 mA cm^{-2} and 0.44 A mg_{Pt}^{-1}. PtCu/CuNWs demonstrate enhanced durability over Pt nanoparticle catalysts by maintaining 64.1% of its active surface area after 30 000 cycles between 0.6−1.1 vs RHE at a scan rate of 50 mV s^{-1} in Ar saturated 0.1 M $HClO_4$. Post durability PtCu/CuNWs outperformed the DOE benchmarks with a SA and MA of 1.50 mA cm_{Pt}^{-2} and 0.477 A mg_{Pt}^{-1}.

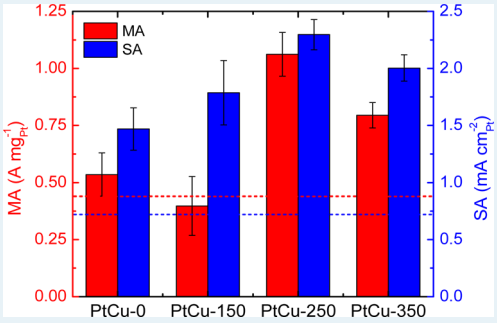

KEYWORDS: *proton exchange membrane fuel cells, ORR catalysts, bimetallic catalysts, core−shell catalysts, extended structure catalysts, dealloyed catalysts*

INTRODUCTION

Proton exchange membrane fuel cells (PEMFCs) are clean, power generation devices that electrochemically combine hydrogen and oxygen via two half reactions: hydrogen oxidation reaction (HOR) and oxygen reduction reaction (ORR). Although high power densities can be achieved using PEMFCs, high loadings of expensive platinum (Pt) catalyst are required due to the slow ORR kinetics, severely limiting PEMFC commercialization.[1] Conventional methods to decrease Pt usage include carbon-supported nanoparticles; however, these are currently unable to meet the activity and durability requirements as set by Department of Energy (DOE) (precious metal mass activity (MA) of 0.44 A mg_{Pt}^{-1} (2017−2020) and specific activity (SA) of 0.72 mA cm^{-2} (2010−2015)).[2,3] The durability of supported catalysts are limited by the corrosion of the carbon support and the loss of Pt surface area through: coarsening (Ostwald ripening), coalescence (Smoluchowski ripening), and dissolution of Pt nanoparticles.[4,5] Consequently, new promising catalysts are required to be cheaper, more active, and more durable than the conventional carbon-supported nanoparticles.

Because breakdown of the carbon support is the main degradation pathway in carbon-supported catalysts, the use of new supports or a supportless catalyst may provide the necessary durability.[5−7] Indeed, first generation supportless catalysts have shown improved durability (e.g., Pt-black) but demonstrate a low mass activity.[7] More advanced supportless Pt nanotubes (PtNT), generated from galvanic displacement of nonprecious metal-based nanowires (CuNW) have shown superior stability over Pt-black.[7,8] Furthermore, the extended surface of the resulting PtNT(Cu) provides a higher SA, attributed to the bulk Pt-like structure.[7−9] PtNT(Cu) met the DOE SA target,[8] but its low Pt utilization resulted in a MA below the DOE benchmark. To increase Pt utilization, a partial galvanic displacement of CuNWs was used to form Pt coated CuNWs (Pt/CuNW). An optimum Pt content of 18 wt % was chosen, resulting in a continuous coating with a minimum amount of Pt (theoretical Pt thickness of 2 nm or 14 monolayers).[8] The continuous Pt coating enhances each of the following: SA by providing a bulk Pt-like extended surface; MA by lowering the overall Pt content; and durability by preventing acid leaching of vulnerable underlying Cu.[8]

Although both the SA and MA are improved, bimetallic systems such as the Pt/CuNW have the potential for even further enhancement in activity. Density functional theory (DFT) calculations showed that ORR activity can be improved by reducing the Pt−O binding energy.[10] The three primary mechanisms that bimetallic systems utilize to improve ORR

Received: May 21, 2014
Revised: July 31, 2014
Published: August 11, 2014

   dx.doi.org/10.1021/cs500692y | ACS Catal. 2014, 4, 3145−3151

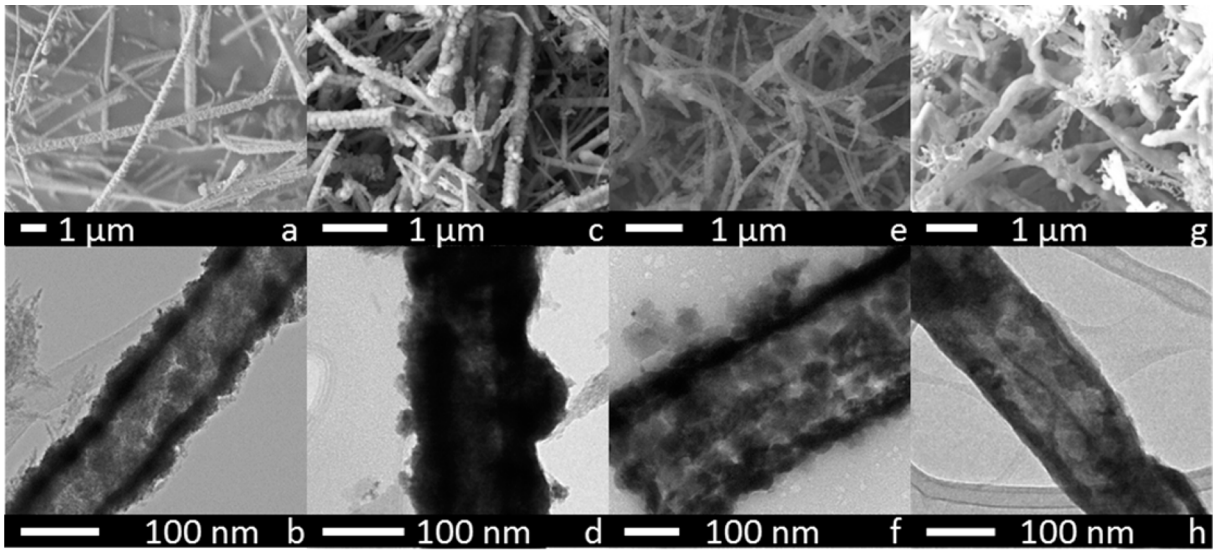

Figure 1. SEM and TEM images of PtCu/CuNWs: PtCu-0 (a,b), PtCu-150 (c,d), PtCu-250 (e,f), and PtCu-350 (g,h).

activity are ensemble, ligand, and geometric effects.[7,11−13] The ensemble effect occurs when discrete surface atoms take on distinctive mechanistic functionalities.[13,14] Ligand effects are brought on by dissimilar atoms in a neighboring atomic position inducing electronic charge transfer and altering the d-band structure.[15] Geometric effects are caused by the change in electronic structure that results from surface strain (compression or expansion) brought on by atoms of different atomic sizes in a crystal lattice.[15−17] Ensemble and ligand effects are only applicable in a bimetallic coordination of less than a few monolayers.[13] Therefore, the only feasible mechanism applicable in the Pt/CuNW system would be geometric tuning. Strasser et al. has demonstrated that an optimal strain exists to boost Pt activity with Cu.[13] Specifically, Cu introduces a compressive lattice strain which shifts the d-band center down, causing a decrease in the adsorption energy between Pt and oxygen.[13,15,16]

In this study, we explored compressive strain's effects on the ORR activity of Pt/CuNWs. We used postsynthetic annealing and electrochemical dealloying to generate a PtCu alloy on the surface of the CuNWs (PtCu/CuNW). Low (150 °C), medium (250 °C), and high (350 °C) annealing temperatures were chosen to control of the degree of diffusion between surface Pt atoms and the underlying Cu, consequently varying the amount of compressive strain in each system. Afterward, electrochemical dealloying of the PtCu/CuNW removed surface Cu, increasing the amount of active Pt surface exposed on the nanowire, while maintaining the strain induced from the alloy. The strain is retained due to the rapid progression of the dealloying process, which does not allow the Pt surface to relax from the strained state.[17] The dealloying also acts to increase the surface roughness and thus the electrochemical surface area (ECSA).[17,18]

■ EXPERIMENTAL SECTION

CuNWs were synthesized through the reduction of precursor copper (Cu) nitrate by hydrazine (N_2H_4, 35 wt %) in the presence of shap-directing ethylenediamine (EDA) and sodium hydroxide (NaOH).[19,20] A Cu nitrate solution (241.6 mg in 10 mL water) was added to 200 mL of 10 M NaOH in a 500 mL reaction vessel. Next, 1.5 mL of EDA and 0.25 mL hydrazine were added sequentially. After each addition, the vessel was capped and vigorously shaken to ensure the even distribution of the reactants. The reaction vessel was placed in a 65 °C water bath for 45 min. The resulting product was then cooled in an ice bath and filtered. Filtering continued until the effluent showed a neutral pH. The product was collected off the filter cake and stored in a vacuum desiccator.

Pt/CuNWs were synthesized through a partial galvanic displacement with CuNWs.[8] A solution of dispersed CuNW (8.4 mg in 200 mL of water) was placed in a magnetically stirred 500 mL round-bottom flask with an attached drop funnel containing a chloroplatinic acid solution (3.5 mg in 100 mL of water). The whole system was flushed with argon (Ar) for 10 min prior to the start and throughout the reaction. Chloroplatinic acid was added dropwise at a rate of approximately 1 drop per 3 s. Following the addition, the flask was allowed to sit for 30 min to ensure completion. The generated Pt/CuNWs were filter collected with a 1 M hydrochloric acid wash and excess water washes.

Pt/CuNWs were directly placed into a tube furnace to generate the corresponding postsynthetic annealed PtCu/CuNW samples. The annealing was performed under flowing Ar. The temperature was ramped to the desired temperature over a 30 min time period and maintained there for 2 h. The furnace was allowed to naturally cool overnight under Ar before the product was collected.

Dealloying and rotating disk electrode (RDE) experiments were both conducted in a three-electrode cell equipped with a saturated calomel reference electrode (SCE), Pt wire counter electrode, and a 5 mm glassy carbon working electrode (Pine Instruments). The cell was controlled by a multichannel potentiostat (VMP2, Princeton Applied Research). The working electrode was connected to a modulated speed rotator (Pine Instruments). All tests were performed in 0.1 M $HClO_4$ (diluted from 70% $HClO_4$, EMD Millipore)

Catalyst ink solutions were generated from 0.261 mg mL^{-1} water dispersions of nanowire materials. A thin film catalyst layer was deposited on the working electrode by pipetting three additions of 15 μL of catalyst ink. A final catalyst loading of 60 $\mu g\ cm^{-2}$ (10.8 $\mu g_{Pt}\ cm^{-2}$) was achieved.

dx.doi.org/10.1021/cs500692y | ACS Catal. 2014, 4, 3145−3151

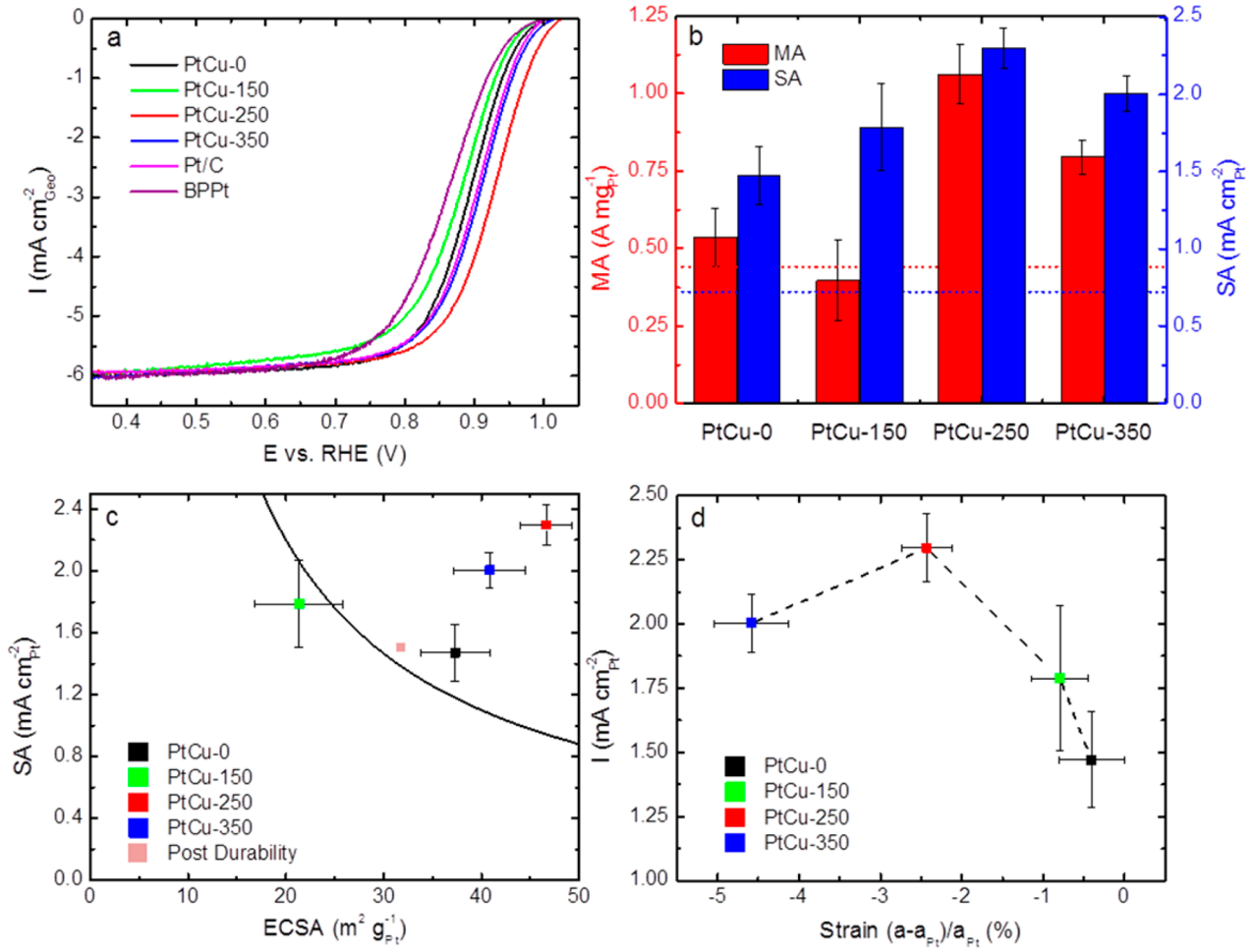

Figure 2. (a) Anodic ORR polarization curves PtCu-(0, 150, 250, 350) as well as Pt/C and bulk polycrystalline Pt (BPPt). ORR scans were taken at 20 mV s^{-1} and 1600 rpm in O_2 saturated 0.1 M $HClO_4$. Currents were normalized to the geometric area of glassy carbon disk electrode. (b) ORR activities for PtCu-(0, 150, 250, 350) normalized to Pt mass and Pt ECSA. DOE targets for MA and SA are denoted by dashed lines. Activities were calculated at 0.9 V vs RHE for the ORR anodic polarization scans at 20 mV s^{-1} and 1600 rpm in O_2 saturated 0.1 M $HClO_4$. (c) SA vs ECSA plot for for PtCu-(0, 150, 250, 350) as well as post durability testing PtCu-250. Determined at 0.9 V vs RHE for the ORR anodic polarization scans at 20 mV s^{-1} and 1600 rpm in O_2 saturated 0.1 M $HClO_4$. Solid line represents the iso-MA line of the DOE MA target of 0.44 A/mg_{Pt}. (d) SA plotted as a function of percentage strain for PtCu-(0, 150, 250, 350). Percent strain was determined by the percent change between the lattice parameters of PtCu samples and the known Pt lattice parameter (3.925 Å). The negative values indicate compressive lattice strain. PtCu lattice parameters were determined from an average of lattice fringe measurements made on TEM micrographs. Cu lattice parameter is 3.619 Å.

Dealloying consisted of a series of cyclic voltammetry (CV) scans in saturated Ar.[5,13,17] Five initial scans were performed at a slow scan rate of 50 mV s^{-1}, to analyze initial Cu stripping characteristics. Subsequently, 200 scans were carried out at an accelerated rate of 200 mV s^{-1} to ensure all surface copper was leached out and a stable CV was obtained.

The ECSA was determined from the double layer corrected average charge of the Pt−hydrogen adsorption and desorption regions between 0.05 V and ∼0.4 V (the onset of the double layer region), assuming a Pt surface charge density of 210 μC cm_{Pt}^{-2}.[21] The measurement was taken at a scan rate of 50 mV s^{-1} in saturated Ar.

ORR measurements were performed at 20 mV s^{-1} in saturated O_2 at a rotation rate of 1600 rpm. The kinetic current (i_k) was calculated by the following equation (eq 1)

$$\frac{1}{i} = \frac{1}{i_k} + \frac{1}{i_d} \quad (1)$$

where i_d is the diffusion limiting current, and i is the measured current. SA was determined from the anodic scan's kinetic current at 0.9 V vs RHE.[21,22]

Scanning electron microscopy (SEM) images and energy-dispersive X-ray spectroscopy (EDS) were taken at 9 kV with a JSM-7400F microscope. Transmission electron microscopy (TEM) images were taken at 200 kV with a JEM-2010F microscope. The TEM samples were prepared by adding a drop of the catalyst suspensions on lacey carbon Cu grids (Ted Pella, Inc.).

RESULTS

The unannealed Pt/CuNWs, low-, medium-, and high-temperature-annealed PtCu/CuNWs, PtCu-(0, 150, 250, 350) respectively, express a diameter of 100 nm and a length of 25−40 μm (Figure 1a−h). The diameter is maintained during the galvanic displacement reaction, but the wire length is reduced from the precursor CuNW's length of 40−50 μm. All of the coated structures contained 18 wt % Pt (remainder: Cu and O), as determined by EDS (Figure S1). EDS has been

dx.doi.org/10.1021/cs500692y | ACS Catal. 2014, 4, 3145−3151

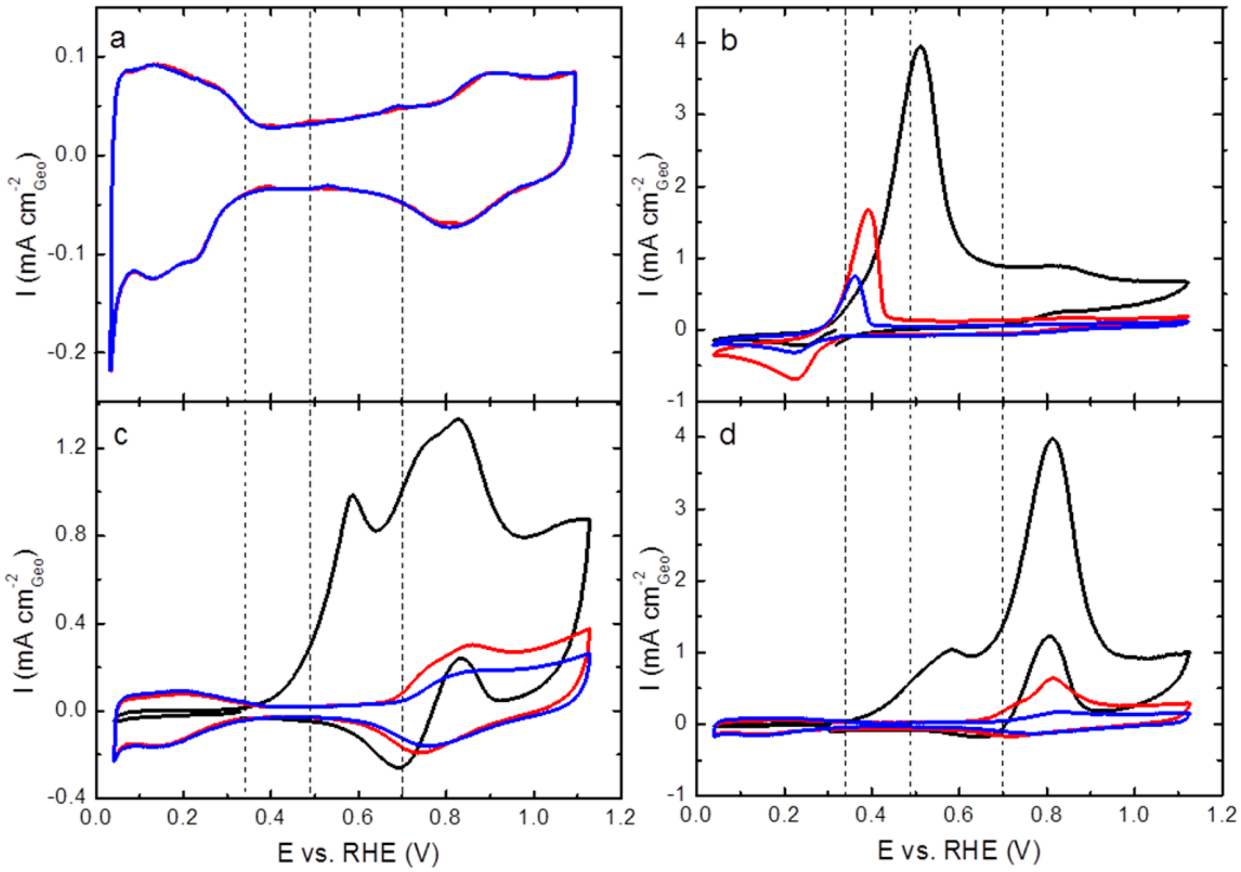

Figure 3. First (black), third (red), and fifth (blue) CV scan for the dealloying process of PtCu-0 (a) and PtCu-150(b), PtCu-250 (c), and PtCu-350 (d). The vertical dashed lines are the thermodynamic minimum potentials for the three model Cu dissolutions (bulk, surface alloy, and monolayer). The current densities are based on the electrode area. CV scans were taken at 50 mV s^{-1} in Ar-saturated 0.1 M $HClO_4$.

validated as an adequate tool for measuring chemical composition in alloyed nanomaterials by ICP in various previous studies.[23,24]

Catalyst ECSAs are calculated from CV curves obtained for all dealloyed structures immediately following the dealloying process (Figure S2). ECSAs for PtCu-(0, 150, 250, 350) are 6.72, 3.84, 8.40, and 7.35 m^2 g^{-1} based on total metal and 37.3 ± 3.5, 21.4 ± 4.5, 46.7 ± 2.6, and 40.8 ± 3.7 m^2 g_{Pt}^{-1} based on Pt. PtCu-0, which underwent no postsynthesis annealing processing, demonstrates a moderate ECSA. This is explained by the intrinsic surface roughness produced by the galvanic displacement reaction. The ECSA value agrees with the previously reported value for Pt/CuNWs.[8] PtCu-150 shows a decrease in the ECSA from the unprocessed wire, likely due to a reduction of surface roughness caused during the low temperature annealing. PtCu-250 demonstrates the highest ECSA owing to the formation of surface pores and roughness introduced during the annealing and dealloying process.[18] The ECSA of PtCu-350 still benefits from the surface roughening, but the agglomeration of the nanowires during the high temperature annealing slightly decreases it from that of the PtCu-250 sample. Due to this reason, higher annealing temperatures were not preferred.

Anodic ORR polarization curves are obtained for PtCu-(0, 150, 250, 350) (Figure 2a) from which MA (Pt mass) and SA (surface area of Pt) were determined (Figure 2b). PtCu-250 demonstrated the highest performance with a SA of 2.30 mA cm^{-2} and MA of 1.06 A mg^{-1}, which enhanced the ORR activity of PtCu-0 SA by 64% (1.47 mA cm^{-2}) and MA by 50% (0.535 A mg^{-1}). This catalyst also outperforms the DOE SA and MA target by a factor of 3.2 and 2.4, respectively.

Accelerated durability tests are conducted via potential cycling at 50 mV s^{-1} between 0.6 and 1.1 V vs RHE. ECSA measurements are taken after 500, 1000, and 5000 cycles and afterward, at every 5000 cycles until 30 000 cycles are reached (Figure S3). PtCu-250 maintained 64.1% of its surface area compared to PtCu-0's 62.3% retention.[8] The ECSA loss is due to the reduction of surface roughness through Pt surface atom migration and Pt dissolution. Post durability SEM demonstrates that the wire morphology is maintained (Figure S4). A 2.7 wt % decrease of Cu in the post durability sample is observed for PtCu-250 (Figure S1). Therefore, Cu dissolution is not expected to cause major performance loss for the membrane and ionomer during fuel cell operation. Supportless PtCu-250 catalyst shows a higher durability than Pt/C, which demonstrates lower ECSA retention, 54.1%.[8] The enhanced robustness is credited to the elimination of carbon support and the resistance to Pt degradation caused by the extended Pt structure. PtCu-250 also exhibits an enhanced stability over dealloyed PtCu/C nanoparticles, allowing it to maintain performance in an ink state for 9 months (Figure S5).[25]

The SAs of PtCu-(0, 150, 250, 350) as well as post durability PtCu-250 are plotted as a function of ECSA (Figure 2c), with the iso-MA line representing the DOE 2017−2020 MA target. Points to the upper right of the iso-MA line surpass the DOE MA target. All but the PtCu-150 exceed the DOE MA target; this is due to the low ECSA of PtCu-150. PtCu-250 allows for the best utilization of Pt enabling it to achieve both a high SA

dx.doi.org/10.1021/cs500692y | ACS Catal. 2014, 4, 3145−3151

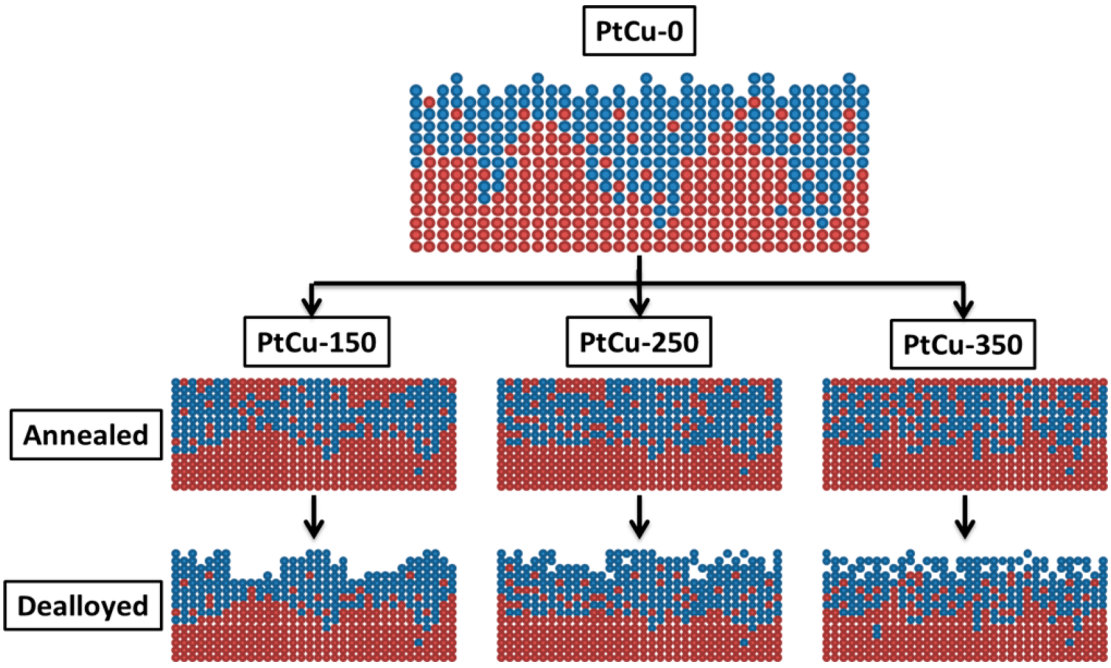

Figure 4. Schematic of the structural evolution of PtCu/CuNWs from as-synthesized Pt/CuNWs (PtCu-0) to the annealed and dealloyed samples at the three strain regimes: low (PtCu-150), medium (PtCu-250), and high (PtCu-350) (Red circles − Cu; blue circles −Pt).

and MA. PtCu-250, even after the durability test, maintains a SA (1.50 mA cm^{-2}), exceeding the DOE SA target, and this combined with its high retention of ECSA leads to a post durability MA (0.477 A mg^{-1}) above the DOE target. Post durability PtCu-250 shows a MA and SA similar to fresh PtCu-0. The SA loss is attributed to the slow dissolution of Cu from the Pt lattice.

DISCUSSION

DFT predicted that Pt ORR activity can be improved through the shifting of d-band center. By increasing compressive strain, the d-band shifts away from the Fermi level, resulting in improvements in ORR kinetics. This ORR improvement was previously observed in dealloyed PtCu nanoparticles;[5,13,17] theoretical Pt overlayers on Cu and alloys;[26] unannealed nanowire and nanotube configurations.[8] Consequently, compressive strain was examined as an indicator for d-band center, defined using the percent change in lattice parameter of PtCu samples compared to that of pure Pt (3.925 Å).

Based on the lattice parameters determined from HRTEM, we observed an increase in strain with annealing temperature (Figure 2d). PtCu-0 demonstrated a strain and lattice parameter of −0.38% and 3.91 ± 0.02 Å, respectively; PtCu-150 showed a higher strain of −0.89% and smaller lattice parameter of and 3.89 ± 0.01 Å; PtCu-250 demonstrated a much higher strain and smaller lattice parameter (−2.67% and 3.82 ± 0.02 Å); and PtCu-350 possessed the highest strain and smallest lattice parameter of −4.97% and 3.73 ± 0.03 Å. As the Cu-induced compressive strain increased from PtCu-0 to PtCu-250, ORR activity increased as expected.[13] This is due to the weakening of the Pt−O binding energy, which increases the ease of product formation and desorption.[2,10] However, for PtCu-350, the Pt−O binding energy becomes too weak, limiting reactant binding and resulting in a decrease in ORR activity compared to that of PtCu-250.

Details of the actual surface alloy structure were deduced from the initial dealloying CV scans.[17] Because stripping of Cu occurs at a potential dependent on its coordination with other elements such as Pt, CV scans provided an estimate of the degree of alloying between Cu and Pt at each PtCu surface. For example, onset of bulk Cu dissolution occurs at 0.34 V vs RHE.[27−29] In contrast, the Cu in PtCu surface alloys experiences a stabilizing effect provided by the Pt, which results in an onset Cu dissolution potential between $0.39 < E < 0.49$ V vs RHE,[27] depending on the specific Pt/Cu ratio. The stabilizing effect is maximized for a Cu monolayer with a Pt subsurface, giving an onset dissolution potential of 0.7 vs RHE.[28,29] Thus, surface structural information was inferred by examining the potentials of the Cu dealloying against the known Cu stripping potentials. Figure S6 shows a schematic representation of the dissolution potentials for the different surface structures of Cu.

Figure 3 shows the first, third, and fifth CV scans for PtCu-(0, 150, 250, 350). PtCu-0 showed no sign of Cu dissolution in the initial scans, instead showing dissolution peaks indicative of pure platinum. This behavior suggested that no PtCu alloying is present at the surface of the sample.

The CV scan for PtCu-150, however, showed a large onset dissolution peak in the bulk Cu stripping regime and also a minor peak in the monolayer Cu stripping zone. The existence of monolayer Cu in this sample was attributed to the migration of the bulk Cu onto Pt during the annealing process.[17,28,29] Over the first 5 scans of PtCu-150, the bulk Cu dissolution peak decreased in magnitude, also showing a negative shift in potential. This behavior indicated a pure bulk Cu phase being stripped until only a Pt skin remains, also suggesting a low amount of PtCu alloying at the surface.

For PtCu-250, dissolution peaks were observed in the bulk regime followed by peaks in both the surface alloy and monolayer region. The twin peaks in the monolayer section implies the presence of a range of PtCu compositions in the surface structure. In addition, the broad overall peak pattern, with peaks shifted toward higher potentials, indicated a higher degree of mixing between Pt and Cu during annealing,

dx.doi.org/10.1021/cs500692y | ACS Catal. 2014, 4, 3145−3151

compared to that seen in PtCu-150.[17,27] The subsequent scans showed the Cu monolayer being stripped off, leaving a pure Pt surface.

PtCu-350 expressed a minor peak in the surface alloy section with a primary peak in the monolayer sector. This indicated the highest degree of Cu migration in the samples prepared, suggesting extensive monolayer formation at the surface.[17] The subsequent five scans showed a decrease of the Cu monolayer peak, as expected.

Based on the HRTEM and CV analysis of the PtCu-(0, 150, 250, 350), the following surface structures were proposed for the postsynthesis, annealed, and dealloyed samples (Figure 4). PtCu-0 demonstrates a rough surface covered by Pt bulk with little Cu alloying. After the sample is annealed at 150 °C (e.g., PtCu-150), the Pt expressed on the surface begins to settle into the Cu core, exposing bulk Cu to the surface. The increased annealing temperature of PtCu-250 resulted in higher mixing degrees of Cu and Pt bulk phases. The resulting product shows a stronger alloy formation, supported by the initial CV scans as well as the increased lattice compression. This trend continues as the annealing temperature is further increased. PtCu-350 shows a fully alloyed PtCu surface partially encapsulated by monolayer Cu.

The dealloying for all three annealed samples strips away any surface Cu, leaving only an exposed Pt surface. For PtCu-150, a reduction in ECSA is observed because the Pt surface unearthed after bulk Cu stripping is smoother. Meanwhile, the PtCu-(250,350) showed an enhanced roughness due to the greater amount of surface-alloyed Cu stripped, leaving behind surface pores.

CONCLUSIONS

By incorporating postsynthesis processing (annealing and dealloying) into the synthesis of Pt/CuNWs (PtCu-0), a high-performance ORR catalyst with the ability to control induced lattice compression was obtained. These results show that tuning compressive strain in a Pt catalyst can optimize the Pt−O binding energy. Of the samples tested, PtCu-250 possessed the highest performance. Its compressive strain and low Pt content displayed a SA and MA of 2.30 mA cm^{-2} and 1.06 A mg^{-1}, respectively, surpassing the previously reported Pt/CuNWs and DOE activity targets. In addition, PtCu-250 maintained a high SA and ECSA, outperforming the DOE MA goals even after postdurability testing.

Analysis of lattice parameters and dealloying CVs showed that Pt/Cu mixing scaled with annealing temperature. Using this knowledge, surface structures were proposed for each PtCu sample, with PtCu-0 having the least Pt/Cu mixing and PtCu-350 displaying the most.

Ultimately, the simple, solution-based CuNW synthesis, coupled with the rapid Pt partial galvanic displacement and facile postsynthesis processing enhances prospects of the PtCu/CuNW catalyst for large scale commercial use in PEMFCs. However, application of these PtCu/CuNW catalysts is not limited to PEMFCs and may prove useful in other reactions, including the methanol oxidation reaction (MOR) and HOR in both acid and base. Furthermore, the concept of controlling compressive strain to tune the binding energy is quite general and may prove insightful for future bimetallic catalysts.

ASSOCIATED CONTENT

Supporting Information

Composition of catalysts determined by EDS, post dealloying CV, ECSA retention relative to initial ECSA, stability analysis, and schematic illustration of Cu dissolution types. This material is available free of charge via the Internet at http://pubs.acs.org.

AUTHOR INFORMATION

Corresponding Author

*E-mail: yanys@udel.edu. Fax: 302.831.2582.

Notes

The authors declare no competing financial interest.

ACKNOWLEDGMENTS

This work was supported by the U.S. Department of Energy through the Fuel Cell Technologies Program under Contract No. DE-AC36-08-GO28308 with the National Renewable Energy Laboratory. This work is benefited by the discussion and training of Kurt Jensen, Shaun M. Alia, and Wenchao Sheng, as well as through the microscopy assistance provided by Zhongbin Zhuang, Min-Rui Gao, and Fei Deng.

REFERENCES

(1) Borup, R.; Meyers, J.; Pivovar, B.; Kim, Y.-S.; Mukundan, R.; Garland, N.; Myers, D.; et al. *Chem. Rev.* **2007**, *107*, 3904−3951.
(2) Gasteiger, H. A.; Kocha, S. S.; Sompalli, B.; Wagner, F. T. *Appl. Catal., B* **2005**, *56*, 9−35.
(3) Gasteiger, H. A.; Panels, J. E.; Yan, S. G. *J. Power Sources* **2004**, *127*, 162−171.
(4) Darling, R. M.; Meyers, J. P. *J. Electrochem. Soc.* **2003**, *150*, A1523.
(5) Hasché, F.; Oezaslan, M.; Strasser, P. *ChemCatChem* **2011**, *3*, 1805−1813.
(6) Lee, K.; Zhang, J.; Wang, H.; Wilkinson, D. P. *J. Appl. Electrochem.* **2006**, *36*, 507−522.
(7) Chen, Z.; Waje, M.; Li, W.; Yan, Y. *Angew. Chem.* **2007**, *119*, 4138−4141.
(8) Alia, S. M.; Jensen, K.; Contreras, C.; Garzon, F.; Pivovar, B.; Yan, Y. *ACS Catal.* **2013**, *3*, 358−362.
(9) Alia, S. M.; Zhang, G.; Kisailus, D.; Li, D.; Gu, S.; Jensen, K.; Yan, Y. *Adv. Funct. Mater.* **2010**, *20*, 3742−3746.
(10) Norskov, J. K.; Rossmeisl, J.; Logadottir, A.; Lindqvist, L.; Kitchin, J. R.; Bligaard, T.; Jonsson, H. *J. Phys. Chem. B* **2004**, *108*, 17886−17892.
(11) Greeley, J.; Stephens, I. E. L.; Bondarenko, A. S.; Johansson, T. P.; Hansen, H. A.; Jaramillo, T. F.; Rossmeisl, J.; Chorkendorff, I.; Norskov, J. K. *Nat. Chem.* **2009**, *1*, 552−556.
(12) Rodriguez, J. A. *Surf. Sci. Rep.* **1996**, *24*, 225−287.
(13) Strasser, P.; Koh, S.; Anniyev, T.; Greeley, J.; More, K.; Yu, C. F.; Liu, Z. C.; Kaya, S.; Nordlund, D.; Ogasawara, H.; Toney, M. F.; Nilsson, A. *Nat. Chem.* **2010**, *2*, 454−460.
(14) Maroun, F.; Ozanam, F.; Magnussen, O. M.; Behm, R. J. *Science* **2001**, *293*, 1811−1814.
(15) Kitchin, J. R.; Norskov, J. K.; Barteau, M. A.; Chen, J. G. *Phys. Rev. Lett.* **2004**, 93.
(16) Mavrikakis, M.; Hammer, B.; Norskov, J. K. *Phys. Rev. Lett.* **1998**, *81*, 2819−2822.
(17) Strasser, P.; Koh, S.; Yu, C. *ECS Trans.* **2007**, *11*, 167−180.
(18) Erlebacher, J.; Aziz, M. J.; Karma, A.; Dimitrov, N.; Sieradzki, K. *Nature* **2001**, *410*, 450−453.
(19) Chang, Y.; Lye, M. L.; Zeng, H. C. *Langmuir* **2005**, *21*, 3746−3748.
(20) Rathmell, A. R.; Bergin, S. M.; Hua, Y. L.; Li, Z. Y.; Wiley, B. J. *Adv. Mater.* **2010**, *22*, 3558−3563.
(21) Garsany, Y.; Baturina, O. A.; Swider-Lyons, K. E.; Kocha, S. S. *Anal. Chem.* **2010**, *82*, 6321−6328.

(22) Takahashi, I.; Kocha, S. S. *J. Power Sources* **2010**, *195*, 6312−6322.
(23) Mani, P.; Srivastava, R.; Strasser, P. *J. Phys. Chem. C* **2008**, *112*, 2770−2778.
(24) Alia, S. M.; Pivovar, B. S.; Yan, Y. S. *J. Am. Chem. Soc.* **2013**, *135*, 13473−13478.
(25) Koh, S.; Strasser, P. *J. Electrochem. Soc.* **2010**, *157*, B585.
(26) Ruban, A.; Hammer, B.; Stoltze, P.; Skriver, H. L.; Norskov, J. K. *J. Mol. Catal. A: Chem.* **1997**, *115*, 421−429.
(27) Greeley, J.; Nørskov, J. K. *Electrochim. Acta* **2007**, *52*, 5829−5836.
(28) Markovic, N.; Ross, P. N. *Langmuir* **1993**, *9*, 580−590.
(29) Markovic, N. M.; Gasteiger, H. A.; Ross, P. N. *Langmuir* **1995**, *11*, 4098−4108.